Title

Transient behavior of a supersonic three-dimensional micronozzle with an intersecting capillary

Journal

Journal of Applied Physics, 119(7)

ISSN

0021-8979

Authors

Matlis, NH

Gonsalves, AJ

Steinke, S

et al.

Publication Date

2016-02-21

DOI

10.1063/1.4940956

AIP | Journal of Applied Physics

Transient behavior of a supersonic three-dimensional micronozzle with an intersecting capillary

N. H. Matlis, A. J. Gonsalves, S. Steinke, J. van Tilborg, B. Shaw, D. E. Mittelberger, C. G. R. Geddes, and W. P. Leemans

Citation: Journal of Applied Physics **119**, 074501 (2016); doi: 10.1063/1.4940956
View online: http://dx.doi.org/10.1063/1.4940956
View Table of Contents: http://scitation.aip.org/content/aip/journal/jap/119/7?ver=pdfcov
Published by the AIP Publishing

Transient behavior of a supersonic three-dimensional micronozzle with an intersecting capillary

N. H. Matlis,[1,a)] A. J. Gonsalves,[1] S. Steinke,[1] J. van Tilborg,[1] B. Shaw,[1] D. E. Mittelberger,[1] C. G. R. Geddes,[1] and W. P. Leemans[1,2]
[1]*Lawrence Berkeley National Laboratory, Berkeley, California 94720, USA*
[2]*Department of Physics, University of California, Berkeley, California 94720, USA*

(Received 13 September 2015; accepted 16 January 2016; published online 16 February 2016)

An analysis of the interaction between a pulsed, supersonic microjet and an intersecting gas-filled capillary is presented, which enables a direct measurement of the pressure evolution inside the nozzle of the microjet. Plasma-emission spectroscopy was used to resolve, on a sub-microsecond timescale, the build-up and decay of pressure in the nozzle, which are shown to be correlated to the volume of the plenum supplying the nozzle and to the nozzle-throat size, respectively. The microjet, which was integrated with a capillary-discharge waveguide in a sapphire structure, was used to create a small, tunable region of high density gas within a centimeter-scale plateau of lower-density for use in a laser-plasma accelerator. The resultant longitudinally structured gas-density profile has been used to provide control of electron trapping and acceleration, but its evolution has not previously been directly quantified. The results presented here pave the way for improved control of laser-plasma accelerators and are also relevant to applications such as miniature satellites and lab-on-a-chip where precise knowledge of microjet pressure evolution is critical. © *2016 AIP Publishing LLC*.
[http://dx.doi.org/10.1063/1.4940956]

I. INTRODUCTION

Micro-sized components for controlling fluid flow, such as micronozzles, have become increasingly important for a wide range of applications, including miniature satellites ("nanosats"),[1] lab-on-a-chip (LOC) devices,[2] and laser plasma accelerators (LPAs).[15–17] The behavior of fluid flow in supersonic micronozzles, which are sub-millimeter-scale converging-diverging (CD) nozzles, can be significantly different than in corresponding macroscopic nozzles, due to changes in the relative importance of the viscous forces.[1] For example, the subsonic layer can occupy a larger percentage of the flow field than in macroscopic counterparts.[5] The small dimensions and volumes of these devices, however, which make use of standard macroscale sensors impossible, present significant challenges for characterization of flow parameters, resulting in uncertainties that can significantly affect the performance of the devices that use them.[1,2] In particular, there is a need to understand transient effects, since pulsed operation is often a key aspect of the use of micronozzles (for example, in nanosats, to control the low levels of impulse required for orbital maneuvering and station-keeping[1] and in LPAs, to control the degree of gas loading in the vacuum chambers). While the flow properties of 2D micronozzles[6] (which converge in only one dimension), and of 3D microjets outside the nozzle[7] have been successfully studied in some detail (due to the transverse access they offer to optical probes), the flow properties of 3D micronozzles within the nozzle are significantly more difficult to probe. The development of methods to characterize critical flow parameters, like pressure and temperature, for 3D supersonic micronozzles is thus currently an active area of research.

In LPAs, supersonic micronozzles are used to control the longitudinal density profile of the gas target. By integrating a micronozzle into a capillary-discharge waveguide, a localized, tunable region of high density connected to a uniform, centimeter-scale region of lower density can be produced, which has been recently shown to be effective for controlling electron injection and acceleration.[3,4] While this concept has been successfully implemented, neither the jet-pressure temporal evolution nor the interaction of the jet with the capillary gas has ever been precisely characterized or described. The behavior of supersonic CD nozzles in steady state is often estimated by using equations describing isentropic expansion of an ideal gas in a cylindrically symmetric nozzle where the nozzle profile is precisely known.[8] In our target, however, the embedded nozzle and capillary waveguide were laser-machined in a sapphire block, resulting in a nozzle geometry which deviates significantly from cylindrical and possesses various non-conical features as a result of the machining process. In addition, the pulsing of the jet gas introduces a dynamic variation in the pressure applied to the CD nozzle which drives an evolution of the jet properties. Isentropic estimates of the jet properties, based on the backing pressure, P_{He}, are therefore unreliable, and an alternate method, capable of resolving the jet evolution, is required. Here, we present a detailed physical description of the jet-capillary interaction cycle and identify key aspects of the interaction which enable direct sensing of the micronozzle pressure and its evolution at the jet-capillary intersection.

II. EXPERIMENTAL SETUP

Experiments were performed in the BELLA center at Lawrence Berkeley National Laboratory. A 250 μm diameter

[a)]Electronic mail: nmatlis@gmail.com

capillary waveguide and supersonic jet nozzle were laser-machined onto sapphire plates (Fig. 1) using an on-site facility.[3] A continuous-flow controller at pressure $P_{H_2} = 50 - 200$ Torr was used to supply hydrogen (H_2) gas to the capillary via two curved slots of cross-sectional area 0.5 mm^2, which intersected the capillary 25 mm apart. The supersonic CD nozzle, with a throat diameter of 570 μm and a 6° expansion cone, was machined transversely to the capillary between the capillary entrance and the first fill slot. The capillary intersected the expansion section 1.2 mm from the throat. A high-speed valve[9] was used to pulse helium (He) with pressure $P_{He} = 0 - 50$ psi (gauge) into a "plenum" which supplied the backing pressure for the nozzle. The plenum consisted of a section of 3/16-in. inner diameter pneumatic tubing, the jet supply slot, and various connectors. Pneumatic tubes of length 3 in. and 6 in. were used to test the effect of plenum volume on the device dynamics. An independently pumped exhaust channel connected to the nozzle was used to evacuate and ensure supersonic operation of the jet. The condition to reach supersonic operation[8] (i.e., choked flow) for ideal monoatomic gases like He, which have an adiabatic index of $\gamma = 5/3$, is $P_{amb}/P_{He} < 0.487$, where P_{amb} is the ambient pressure in the nozzle before the jet fires. Assuming there is sufficient time between shots for the plenum to evacuate through the exhaust, P_{amb} is a result of H_2 leaking from the capillary. It is thus expected that $P_{amb} < P_{H2} \ll P_{He}$, and that the nozzle is supersonic for all combinations of P_{He} and P_{H2} used.

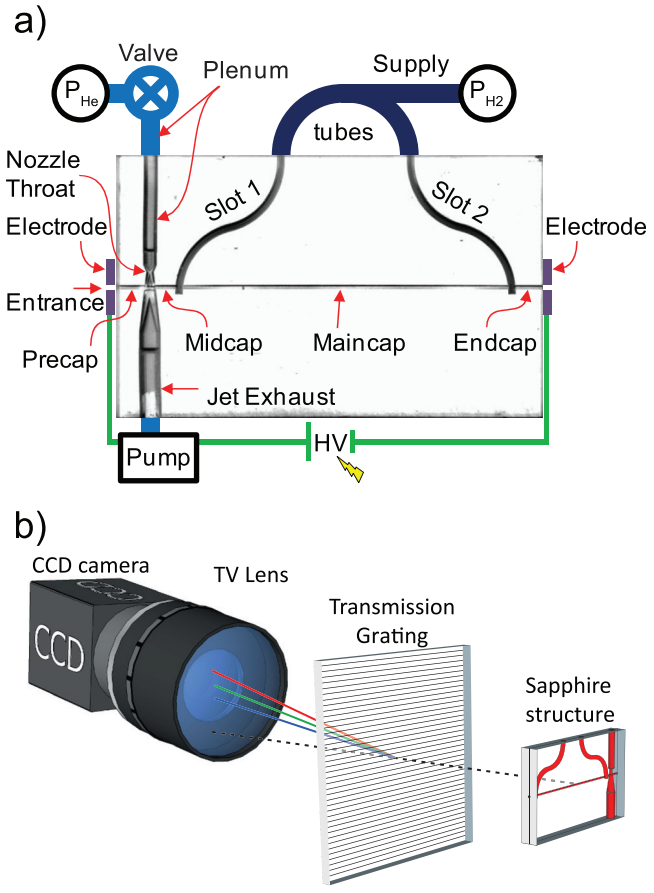

FIG. 1. (a) Diagram of the integrated capillary waveguide and supersonic jet structure. (b) Schematic of spectrometer. Three diffracted rays of red, green, and blue represent dispersion of the light from the sapphire structure.

A 100–150 A, 200 ns current pulse was used to ionize gas in the capillary and jet to form the optical waveguide.[10] Plasma recombination light scattered by the capillary and jet surfaces was collected by a custom imaging spectrometer designed to produce distinct replicas of the structure for each of the emission wavelengths. As a result, two-dimensional intensity distributions of the emission lines for H_2 (656.3 nm, H_α) and He (587.6 nm, D_3) were captured simultaneously (Fig. 2(a)). The use of distinct gases for the jet and capillary allowed the two sources to be distinguished by their emission signature. Although the exposure time of the camera was set to 100 ms, the time resolution of the technique was determined by the recombination time of the plasma, which was measured to be of the same order as the duration of the current pulse, i.e., 200 – 300 ns. The camera thus integrated over the entire lifetime of the plasma emission. However, since the emission time scale is much shorter than any time scale of the neutral fluid motion, the discharge acted as a strobe, so that the resulting images were of the (effectively) instantaneous spatial distributions of the neutral He and H_2. The dynamics of the interaction between the two gases was then captured by varying the timing delay, t, between the discharge and the jet trigger.

III. ANALYSIS

Before the jet fires, H_2 flows steadily through the fill slots to the capillary, and then through the Endcap and

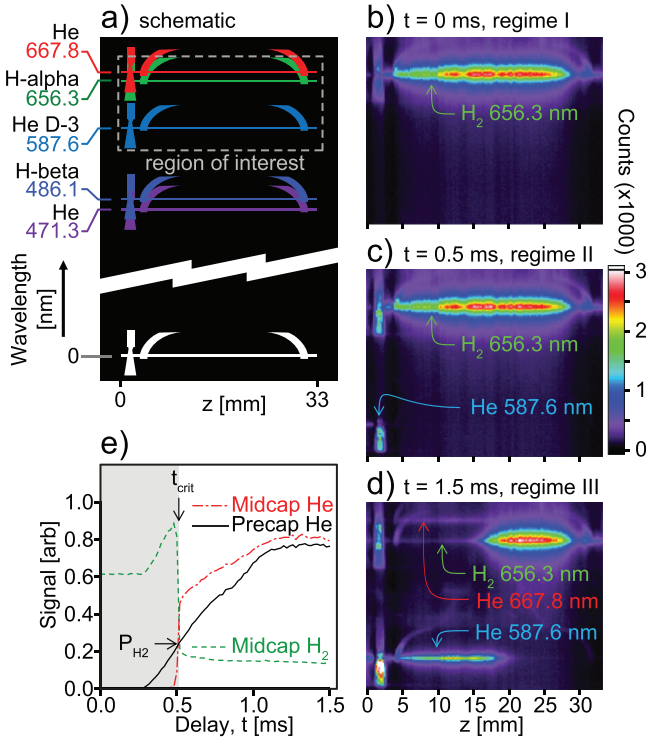

FIG. 2. (a) Conceptual depiction of spectrally dispersed image showing sapphire structure represented by multiple hydrogen and helium emission lines. (b)–(d) Spectrometer images corresponding to region of interest in (a) showing the hydrogen H_α (656.3 nm) and helium D_3 (587.6 nm) emission lines for discharge delays of 0 ms, 0.5 ms, and 1.5 ms, respectively, at $P_{He} = 50$ psi (gauge) and $P_{H_2} = 100$ Torr. (e) Precap helium (black solid line), Midcap helium (red dotted-dashed line), and Midcap hydrogen (green dashed line) signals. The arrows indicate the location of the reference point on the Precap He signal.

Midcap. The fill slots and other H_2 delivery tubes were designed to minimize pressure loss between the source at P_{H_2} and the capillary at P_{cap}, so that $P_{cap} \approx P_{H_2}$, to within about 1%. Since the pressure supplied by both slots is the same, there is no flow across the Maincap, and thus a region of constant density is provided. The flow through the Midcap and Endcap, however, results in pressure and density gradients in these sections.[11,12] Most of the gas exiting the Midcap flows down the jet exhaust rather than into the Precap, due to the former's much-larger diameter. Figure 2(b) shows a spectrometer image taken just before the jet fires. The H_2 emission line is visible, illuminating the entire structure, while the He line is completely absent. The longitudinal variations in the H_2-line brightness are caused by variations in both the output coupling and the light collection efficiency.

Once the valve triggers, high-pressure He rushes into the plenum, filling it on a ~1 ms timescale. If the valve is open sufficiently long, the plenum pressure equilibrates with P_{He}, since the valve orifice is much larger than the nozzle orifice. Once the valve closes, the plenum pressure then drops as gas escapes through the nozzle orifice. The jet pressure, $P_{jet}(t)$, which corresponds to the pressure in the nozzle where it intersects the capillary, tracks the evolution of the plenum pressure, but is significantly lower due to the effects of expansion in the nozzle. The pressure gradient and therefore the flow in the Midcap react in turn to the evolving jet pressure. As the jet pressure rises, the pressure difference, $\Delta P(t) \equiv P_{jet}(t) - P_{cap}$, can change sign, causing the flow in the Midcap to reverse direction. During reversed flow, He from the jet displaces H_2, first in the Midcap and then in the fill slots and Maincap. Figure 2(c) shows a spectrometer image just before the flow reverses direction. The H_2-line distribution is relatively unchanged, compared to Figure 2(a), but the He line has appeared, localized to the jet, the jet exhaust, and the Precap. Figure 2(d) shows a spectrometer image just after the flow reversal, and the displacement of H_2 by He can be seen by the extension of the He line into the Maincap and the matching regression of the H_2 line.

The flow reversal during the jet-pressure buildup provides a mechanism for directly calibrating the jet pressure. Since the jet and the capillary are supplied by different gases, the flow reversal causes a very sudden change in the Midcap gas composition. This change can be readily identified in the signals corresponding to the line-emission brightness of the two gases in that region. Figure 2(e) shows the He and H_2 line brightnesses integrated over a portion of the Midcap (red-solid and green-dotted lines, respectively). A sharp upward transition in the He signal from the Midcap, $S^{He}_{Midcap}(t)$, indicates the "critical" moment, $t = t_{crit}$, when the jet pressure equals the capillary pressure ($P_{jet} = P_{cap}$). The corresponding sharp downward transition in the H_2 signal, $S^{H_2}_{Midcap}(t)$, shows that the H_2 gets displaced by the He. Since $P_{cap} \approx P_{H_2}$, the pressure of the jet at the critical time, $P_{jet}(t_{crit})$, can be approximated by the known H_2 set pressure, P_{H_2}. The transition analysis thus provided a direct measurement of both a time and a pressure, which define a reference point on the $P_{jet}(t)$ curve. Since the transition occurs at later times for higher capillary pressures (Fig. 3(a)), a series of

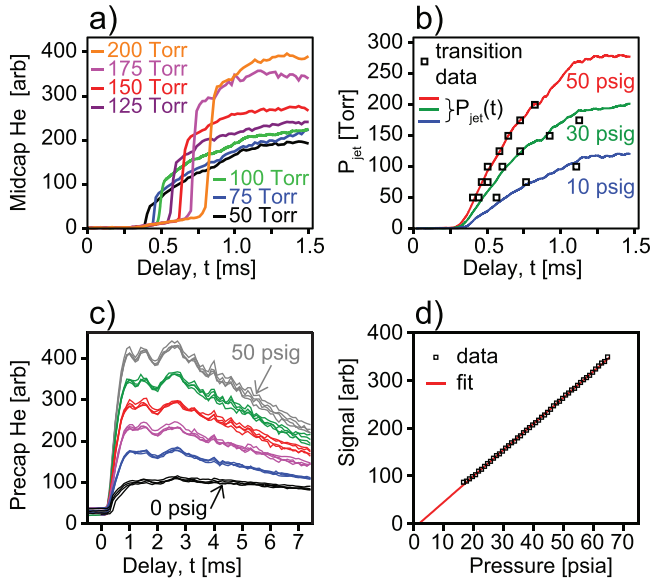

FIG. 3. (a) $S^{He}_{Midcap}(t)$ traces for P_{H_2} from 50 to 200 Torr in 25 Torr increments, with transition features at early times for lower pressures and at progressively later times for higher pressures. (b) Map of Helium pressure curves for P_{He} = 10, 30, 50 psi (gauge). (c) Sets of four $S^{He}_{Precap}(t)$ traces with P_{H_2} varying from 55 to 100 Torr for each of six P_{He} values from 0 to 50 psi (gauge). Each color represents a distinct P_{He}. (d) S^{He}_{Precap} vs P_{He} at t = 3.5 ms. Error bars from averaging over all data sets shown in (c) are too small to be seen.

delay scans with varying P_{H_2} could be used to map out $t_{crit}(P_{H_2})$ which, when inverted, represents $P_{jet}(t)$ (Fig. 3(b)).

A more continuous measurement of the pressure evolution can be obtained from the Precap He signal. In general, the brightness of an emission line depends linearly on the number of emitters, and therefore on the gas pressure, provided that all other parameters are fixed. For the jet, this condition was most closely met by the He signal from the Precap, $S^{He}_{Precap}(t)$ (Fig. 2(e), black-dotted curve). Since the Precap is isolated from the rest of the capillary by the jet exhaust, very little H_2 reaches it, and it is therefore largely unaffected by changes to P_{cap} or by the interaction between the jet and the capillary. In addition, since it is oriented transversely to the motion of the jet gas, the Precap probes the jet static pressure, which is connected to the density via the ideal gas law.

Figure 3(c) confirms that $S^{He}_{Precap}(t)$ depends linearly on P_{He} and is insensitive to P_{H_2} (as evidenced by the overlap of multiple traces of differing P_{H_2}). Figure 3(d) shows a linear fit to S^{He}_{Precap} vs. P_{He} at $t = 3.5$ ms, which indicated an RMS deviation from linear of <2.4%. By normalizing the curves in Fig. 3(c), it was found that the temporal shape of $S^{He}_{Precap}(t)$ was also independent of both P_{He} and P_{H_2} to within an RMS variation of 3.2%, confirming the independence of the Precap from the dynamics occurring in the Midcap. These results show that $S^{He}_{Precap}(t)$ is a suitable signal to represent the jet pressure evolution provided that a calibration can be found. This calibration was determined by scaling $S^{He}_{Precap}(t)$ to fit the $P_{jet}(t)$ data obtained from the flow-reversal analysis above. Figure 3(b) shows that the scaled $S^{He}_{Precap}(t)$ data agree well with the flow-reversal analysis both in temporal dependence and in absolute temporal position.

The calibration enables determination of several key parameters associated with the nozzle, including the degree of

expansion and the jet temperature. The plateau at the top of the $P_{jet}(t)$ curve shows that the plenum pressure, P_{plen}, has equilibrated to the source pressure, P_{He}, providing a direct measurement of the pressure drop caused by the CD nozzle: $P_{jet}/P_{plen} = 0.085$. The jet temperature can then be determined by assuming isentropic expansion of an ideal gas, and assuming the He is initially at room temperature: $T_{jet} = T_{plen}(P_{jet}/P_{plen})^{(\gamma-1)/\gamma} = 111$ K. Similarly, the ratio between the cross-sectional areas of the nozzle at the throat and at the capillary can be inferred: $A_{cap}/A_* \approx 1.81$, where the asterisk refers to quantities at the nozzle throat. For comparison, the area ratio estimated using transverse imaging was $(A_{cap}/A_*)' \approx 2.1$, which results in $(P_{jet}/P_{plen})' = 0.062$ and $T'_{jet} = 98$ K.[13]

Having established $S^{He}_{Precap}(t)$ as a reliable indicator of the jet pressure, it can then be used to characterize the main contributions determining the jet-pressure evolution: the filling of the plenum, while the valve is open, and the emptying of the plenum through the nozzle throat, both of which are affected by the plenum volume. Figure 4(a) shows a comparison between the jet-pressure buildup using the 3- and 6-in. plenum tubes at five different P_{He}. As expected, the larger plenum takes longer to fill and starts filling later. The maximum pressure for both cases is the same, confirming that the calibrations are reliable and that the plenum has, in fact, equilibrated with the source pressure.

Once the valve closes, the plenum pressure decays exponentially due the flow through the nozzle orifice. This decay can be modeled by assuming choked flow (i.e., the flow speed at the throat is locked to the sound speed), resulting in an exponential time constant given by: $\tau = V/\alpha A_* c_{He}$, where V is the plenum volume, $\alpha \equiv \left(\frac{2}{\gamma+1}\right)^{\frac{\gamma-1}{2(\gamma+1)}} \approx 0.56$ for He, and $c_{He} \sim 1,016$ m/s is the He sound speed at room temperature. By accounting for the volume of the components comprising the plenum and using the value of A_* determined from imaging, expected time constants could be calculated for the 3- and 6-in. tubes: $\tau_1^{calc} = 9.6$ ms and $\tau_2^{calc} = 18.8$ ms, respectively. For comparison, the measured time constants, determined by fitting an exponential to the decreasing tail of the $S^{He}_{Precap}(t)$ traces (Fig. 4(b)), were $\tau_1^{meas} = 9.1$ ms and $\tau_2^{meas} = 11.2$ ms, respectively, agreeing well in the shorter-plenum case.

More details about the jet evolution can be determined by taking the numerical derivative of the signal, which represents the rate of change of pressure in the plenum. The exponential fits can then be used to eliminate the contribution to the rate of change from the leakage through the orifice, leaving only the pressure-buildup dynamics. Figure 4(c) shows a comparison of the buildup dynamics for the two plenum sizes. The primary peak between 0 and 1 ms describes the opening and closing of the valve and verifies a sub-ms operation. A slight shift in the peak position between the 3-in. and 6-in. cases is noticeable. A secondary peak between 2 and 3 ms indicates that the impulsively driven valve is most likely bouncing after the initial closure. Superimposed on these features are oscillations which continue for several milliseconds. Comparison of two traces from the 3-in. setup and a third from the 6-in. setup reveals that the oscillations are not noise, but rather most likely result from pressure waves bouncing back and forth in the plenum, since the frequency ratio is approximately that of the tube lengths.

Using the above methodology, it was not possible to resolve the spatial variations of pressure or density within the jet, leading to ambiguities about the values and dynamics of these quantities. To address this issue, a simulation using the ANSYS engineering-simulation platform was performed to characterize the expected gradients for our geometry. Figure 5 shows that in fact both pressure and density vary by less than 10% over the spatial extent of the jet. Thus, while the above analysis pertains strictly to the pressure at the

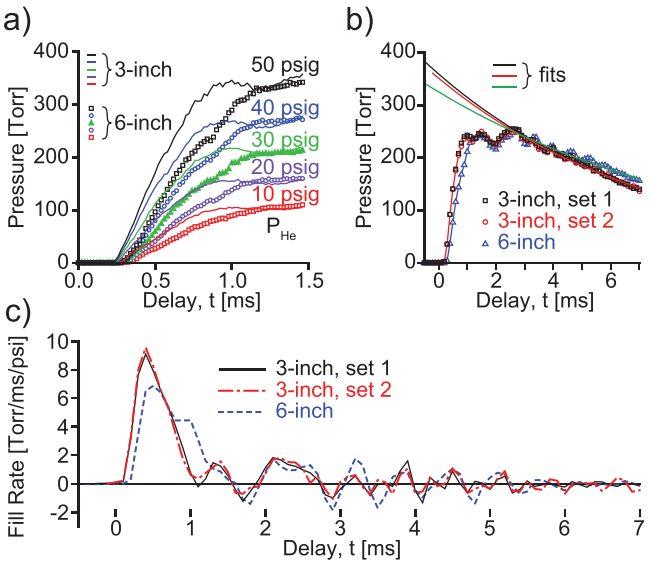

FIG. 4. (a) Rising edge comparison between 3-in. (solid lines) and 6-in. (dotted lines) plena for $P_{He} = 10, 20, 30, 40, 50$ psi (gauge). (b) Falling edge comparison for 3-in. plenum tube (black) and 6-in. plenum tube (blue), and associated exponential fits. (c) Fill rates defined by $dP_{jet}(t)/dt/P_{he}$.

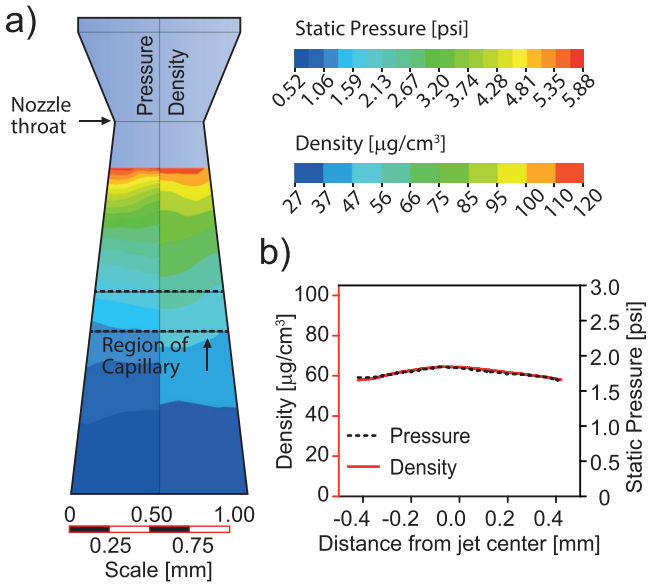

FIG. 5. (a) Results of a steady-state, radially symmetric ANSYS simulation of the jet showing color plots of pressure (left side) and density (right side), for the case of $P_{He} = 30$ psi. (b) Lineouts of the pressure and density in (a) versus transverse position at the location where the capillary intersects the nozzle.

junction between the jet and the capillary, it may be taken as a reasonable approximation to the on-axis behavior as well.

IV. CONCLUSIONS

We have demonstrated a method for characterizing the pressure dynamics within a 3-D, pulsed, supersonic micronozzle by using plasma spectroscopy to resolve the interaction with a transecting, gas-filled capillary. The emission from a particular region of the structure was identified as a reliable, real-time monitor of the instantaneous jet pressure, and a method to calibrate the signal was determined and implemented. The resultant diagnostic was used to resolve the jet-pressure evolution, including build-up and exponential decay as well as oscillations possibly due to pressure waves bouncing in the plenum. The temporal behavior of the pulsing valve, which previously required removing the device, was also determined *in-situ*. This methodology provides a framework for design, development, and operational tuning of a wide range of micro-jet-based devices across a wide range of applications, including LPAs and miniature satellites. The results of this work have subsequently been used to enable the characterization of the longitudinal density profile and dynamics in the capillary section of the device used here.[14] This density information is critical for the implementation of such devices for controlling LPAs.

ACKNOWLEDGMENTS

This work was supported by the Director, Office of Science, Office of High Energy Physics, of the U.S. DOE under Contract No. DE-AC02-05CH11231.

[1]W. F. Louisos and D. L. Hitt, "Transient analysis of supersonic viscous flow in 3D micronozzles," AIAA Paper 2011-3996, 2011.
[2]P. Knapkiewicz and R. Walczak, *Microsensors for Microreaction and Lab-on-a-Chip Applications* (InTech, Rijeka, 2011), pp. 109–142.
[3]A. J. Gonsalves, K. Nakamura, C. Lin, D. Panasenko, S. Shiraishi, T. Sokollik, C. Benedetti, C. B. Schroeder, C. G. R. Geddes, J. van Tilborg, J. Osterhoff, E. Esarey, C. Tóth, and W. P. Leemans, "Tunable laser plasma accelerator based on longitudinal density tailoring," Nat. Phys. **7**, 862–866 (2011).
[4]L. Schaper, L. Goldberg, T. Kleinwächter, J.-P. Schwinkendorf, and J. Osterhoff, "Longitudinal gas-density profilometry for plasma-wakefield acceleration targets," Nucl. Instrum. Methods A **740**, 208–211 (2014).
[5]S. D. Scroggs and G. S. Settles, "An experimental study of supersonic microjets," Exp. Fluids **21**, 401–409 (1996).
[6]C. Huang, J. W. Gregory, and J. P. Sullivan, "Flow visualization and pressure measurement in micronozzles," J. Visualization **10**, 281–288 (2007).
[7]W. R. Lempert, N. Jiang, S. Sethuram, and M. Samimy, "Molecular tagging velocimetry measurements in supersonic microjets," AIAA J. **40**, 1065–1070 (2002).
[8]J. D. Anderson, *Modern Compressible Flow with Historical Perspective*, 3rd ed. (McGraw Hill, 2002).
[9]M. Krishnan, K. W. Elliott, C. G. R. Geddes, R. A. Mourik, W. P. Leemans, H. Murphy, and M. Clover, "Electromagnetically driven, fast opening and closing gas jet valve," Phys. Rev. Spec. Top. - Accel. Beams **14**, 033502 (2011).
[10]W. P. Leemans, B. Nagler, A. J. Gonsalves, C. Tóth, K. Nakamura, C. G. R. Geddes, E. Esarey, C. B. Schroeder, and S. M. Hooker, "GeV electron beams from a centimetre-scale accelerator," Nat. Phys. **2**, 696–699 (2006).
[11]S. Varoutis, D. Valougeorgis, O. Sazhin, and F. Sharipov, "Rarefied gas flow through short tubes into vacuum," J. Vac. Sci. Technol., A **26**, 228–238 (2008).
[12]F. M. Sharipov and V. D. Seleznev, "Rarefied as flow through a long tube at any pressure ratio," J. Vac. Sci. Technol., A **12**, 2933–2935 (1994).
[13]See http://www.engineering.com/calculators/isentropic_flow_relations.htm for "Isentropic flow relations calculator," accessed: 2015-01-15.
[14]N. H. Matlis, A. J. Gonsalves, S. Steinke, J. van Tilborg, E. H. Matlis, B. Shaw, C. G. R. Geddes, and W. P. Leemans, "Dynamics and density distributions in a capillary-discharge waveguide with an embedded supersonic jet," J. Appl. Phys. **118**, 204506 (2015).
[15]T. Tajima and J. M. Dawson, "Laser electron accelerator," Phys. Rev. Lett. **43**, 267–270 (1979).
[16]T. Katsouleas, "Electrons hang ten on laser wake," Nature **431**, 515–516 (2004).
[17]W. Leemans and E. Esarey, "Laser-driven plasma-wave electron accelerators," Phys. Today **62**(3), 44–49 (2009).